Appl Phys B (2010) 101: 849–854
DOI 10.1007/s00340-010-4331-0

Applied Physics B
Lasers and Optics

Size-dependent luminescence of Sm^{3+} doped SnO_2 nano-particles dispersed in sol-gel silica glass

A.C. Yanes · J. Méndez-Ramos · J. del-Castillo · J.J. Velázquez · V.D. Rodríguez

Received: 5 March 2010 / Revised version: 3 November 2010 / Published online: 23 November 2010
© Springer-Verlag 2010

Abstract Sol-gel glasses with composition $(100-x)SiO_2$–$xSnO_2$ doped with 0.4 mol% of Sm^{3+}, with x ranging from 1 to 10, have been successfully synthesized. Transparent doped nano-glass-ceramics were prepared by thermal treatment of the precursor glasses at 900°C during 4 hours, leading to nanocomposites comprising SnO_2 nanocrystals embedded into an amorphous SiO_2 phase. A structural analysis in terms of X-ray Diffraction and High Resolution Transmission Electron Microscopy confirms the precipitation of SnO_2 nanocrystals within the glassy matrix. The mean radius of the obtained SnO_2 nanocrystals, ranging from 2.1 to 4.7 nm calculated by the Scherrer and Brus equations, similar to the Bohr's exciton radius, constitutes a wide band-gap semiconductor quantum-dot system. Energy transfer from SnO_2 nanocrystal host to Sm^{3+} ions is confirmed by luminescence spectra and analyzed as a function of SnO_2 concentration, showing an evolution that could be ascribed to selective excitation of nanocrystal sets with predetermined size. Besides, a study of the luminescence as a function of temperature helps to clarify the involved energy transfer mechanisms.

1 Introduction

Properties of nanoscale dimensioned semiconductors are particularly interesting when the nanoparticle radii are smaller or comparable to the corresponding Bohr's exciton radius [1]. Under these conditions, the semiconductor nanocrystals, known as quantum dots (QDs), exhibit an intermediate behavior between a bulk crystal and an isolated molecule due to quantum-confinement effects [2]. Significant blue-energy shifts of the intrinsic absorption edge and quantization of electronic energy levels can be induced by the strong confinement of the excitons inside the QDs [3].

Nanostructured semiconductor based materials are attractive from a fundamental and technological viewpoint with diverse potential applications, owing to their size-dependent physical properties. Their unique optical properties include strong light absorbance, broad-range excitation, size-tuneable emission spectra (correlation between nanoparticle size and emission wavelength) and elevated photostability. In general, the intrinsic emission of these materials is quite weak at room temperature. Thus, to enhance luminescence, more emissive centers, e.g. rare-earth ions (RE), should be introduced which are efficiently excited through energy transfer from the host. On the other hand, glasses have proved to be useful as host materials for RE elements due to their high transparency, compositional variety and easy mass production. Therefore, nanostructured materials comprising QDs embedded in glassy matrices show promising applications in optical devices.

Among semiconductor materials, tin dioxide (SnO_2) is a wide gap n-type semiconductor (band gap of 3.6 eV at 300 K) presenting a broad range of applications like gas sensors or transparent conducting electrodes and others [4]. Its behavior under UV excitation is especially interesting when doping with RE ions, due to efficient energy transfer from the SnO_2 host to these dopants giving rise to visible emissions [3, 5–7].

Despite the great body of work about RE ions doped semiconductor nanostructures [3, 5–12], there is a need of

A.C. Yanes · J. del-Castillo
Dpto. Física Básica, Universidad de La Laguna, 38206 La Laguna, Tenerife, Spain

J. Méndez-Ramos (✉) · J.J. Velázquez · V.D. Rodríguez
Dpto. Física Fundamental y Experimental, Electrónica y Sistemas, Universidad de La Laguna, 38206 La Laguna, Tenerife, Spain
e-mail: jmendezr@ull.es

a deep understanding of the transfer mechanisms and factors affecting RE ions luminescence features; i.e. host matrix, band gap, site symmetry, etc., in particular in RE doped SnO_2 nanocrystals.

For this aim, Sm^{3+} ions are one of the most interesting lanthanide ions to analyze the fluorescence properties, acting as a spectroscopic probe [11], due to presence of hypersensitive transitions to the symmetry of the ion environment, along with potential application for high-density optical storage and color displays [12]. In this sense, in a previous work we analyzed sol-gel derived nano-glass-ceramics containing Sm^{3+}-doped SnO_2 nanocrystals for a fixed tin oxide concentration [11], indicating the possibility of exciting selectively nanocrystal subsets with a particular size. The sol-gel method provides a simpler room-temperature approach for synthesis of glasses with low cost and homogeneity of final materials at molecular level allowing partition of QDs with controlled size and doping level under adequate heat treatment [5, 6].

Thus, in the present work we study the luminescence of sol-gel derived Sm^{3+}-doped nano-glass-ceramics with different content of SnO_2, which allows us to compare samples with nanocrystal distribution of different mean size. Moreover, the underlying mechanisms of the energy transfer from SnO_2 nanocrystals to the luminescent ions have been analyzed by means of the luminescence evolution with temperature.

2 Experimental

Silica glasses with different concentrations of SnO_2 (1, 3, 5 and 10 mol%) doped with 0.4 mol% of Sm^{3+} were obtained by a sol-gel method using dibutyltin-diacetate DBTDA $Sn(CH_2CH_2CH_2CH_3)_2(OOCCH_3)_2$ and tetraethoxysilane (TEOS) $Si(OCH_2CH_3)_4$ as Sn and Si sources, respectively, as described in [11]. First, TEOS (99.999%) and the required quantity of DBTDA in ethanol solution were hydrolyzed at room temperature by addition of distilled deionized H_2O dropwise under magnetic stirring for 1 h (molar ratio TEOS:H_2O:C_2H_5OH=1:8:5). Afterwards, $Sm(NO_3)_3 \cdot 6H_2O$ (99.9%) dissolved in ethanol was slowly added into the precursors under stirring. A highly transparent gel was obtained by leaving the resultant homogeneous solution in a sealed container at 35°C for several days. Then, the gels were dried by slow evaporation of residual water and solvent. Finally, these xerogels were heat treated in air atmosphere at 900°C for 4 h in order to achieve a stiff glass network and a controlled precipitation of SnO_2 nanocrystals giving rise to transparent nano-glass-ceramics.

X-ray powder diffraction (XRD) patterns of the samples were recorded with a Philips X'Pert Pro diffractometer equipped with a primary monochromator, Cu $K_{\alpha 1,2}$ radiation, and a X'Celerator detector. The XRD patterns were collected with a step of 0.016° in the 2θ angular range 10 to 90° and acquisition time of 2 h. Furthermore, the patterns were corrected by using LaB_6. Transmission Electron Microscopy TEM and HRTEM images were obtained using a JEOL 3010F microscope operated at 300 KV. This microscope is equipped with a Field Emission Gun, which allowed us to achieve a point-to-point resolution of 0.17 nm. Specimens were prepared by dispersing the fine powder obtained by grinding the sample, using a mortar and pestle in acetone with ultrasonic agitation, and then, a droplet of the suspension was put on a copper holey carbon grid. Selected areas of the HRTEM images were mathematically filtered by means of Fast Fourier Transform (FFT) analysis resulting in power spectra patterns. These power spectra correspond to the eigen frequencies of the observed nanocrystals, which were indexed according to the GATAN Digital Micrograph software. Further, the relevant frequencies were selected to filter the noise in the zoomed areas of the HRTEM images and to produce the highest contrast images of observed nanocrystals, determining the atomic planes of these nanocrystals.

Luminescence spectra were obtained by exciting the samples with light from a 300 W Xe arc lamp passed through a 0.25 m double-grating monochromator and detecting with a 0.25 m monochromator with a photomultiplier. Low temperature spectra were acquired by using a He cycling cryogenerator. All spectra were corrected by the instrumental response.

3 Results and discussion

The powder XRD patterns taken from $(100 - x)SiO_2$–$xSnO_2$ nano-glass-ceramics, doped with 0.4 mol% of Sm^{3+}, with $x = 1$, 3, 5 or 10 and heat treated for 4 hours at 900°C, are shown in Fig. 1. Diffraction peaks are observed, due to a crystalline phase, over a broad diffraction band corresponding to the glass matrix. The broadening of diffraction peaks indicates small nanocrystals size. The peaks located out at 26.6, 33.9, 37.9, 51.9, 62.4 and 65.1° can be indexed as SnO_2 cassiterite known from the bulk crystals (JCPDS file 41-1445, also presented in Fig. 1 as vertical bars) without additional crystalline phases. The diffraction curve of the non-heat-treated glassy samples, also included in Fig. 1, shows up their amorphous character without nanocrystals precipitation. The presence of SnO_2 nanocrystals is hardly appreciable in the sample with 1 mol% of SnO_2 meanwhile they are clearly observed with 3 mol% and larger concentrations. The average radius of the nanocrystals was estimated by the Scherrer equation, from diffraction plane (101), to be 2.1, 2.8 and 4.2 nm for samples with 3, 5 and 10 mol% of SnO_2. This value of the mean radius is representative of the complete volume of the bulk sample. It should be noticed the

appreciable increase of the nanocrystal size with the SnO_2 concentration.

Besides, in order to complete the structural and morphological analysis, TEM and HRTEM images were collected for 5 mol% SnO_2 sample, see Fig. 2. The observed nanocrystals in the bright-field micrograph are nearly spherical particles clearly visible as dark spots and homogeneously dispersed in the amorphous silica network, see Fig. 2(a). Moreover, they present a narrow size distribution between 4–6.6 nm in diameter, in good agreement with XRD data. A crystalline nanoparticle can be seen in the HRTEM micrograph shown in Fig. 2(b) marked by white circle. The right-top side inset displays the power spectrum obtained from the same circled nanoparticle. Indexation of the spectrum spots clearly shows that the nanoparticle corresponds to a SnO_2 cassiterite crystal. In addition the right-bottom inset in Fig. 2(b) shows the image of the nanocrystal where direct image was filtered, by using the frequencies determined from the Fast Fourier Transform (FFT) pattern, with the (121) axis parallel to the electron beam.

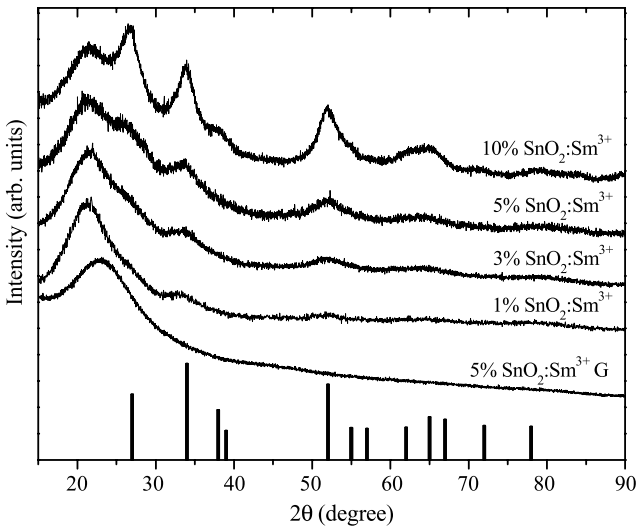

Fig. 1 XRD patterns of $(100 - x)SiO_2$–$xSnO_2$:$0.4Sm^{3+}$ glass-ceramics, with $x = 1$, 3, 5 or 10 mol% of SnO_2 and heat treated during 4 hours at 900°C, along with non-heat-treated glassy sample (G). Bragg peaks corresponding to SnO_2 cassiterite crystals are included as *vertical bars* for comparison (JCPDS file 41-1445)

The evolution of the excitation spectra for SiO_2–SnO_2 samples with different concentrations of SnO_2 (3, 5 and 10 mol%) are presented in Fig. 3, by detecting the Sm^{3+} emission at 567 nm ($^4G_{5/2} \rightarrow {}^6H_{5/2}$ transition). In all spectra a narrow peak located at about 402 nm can be clearly observed together with an intense broad UV band. This narrow peak mainly correspond to direct excitation of the high fraction of Sm^{3+} ions that remain in the glassy phase [11], from the ground $^6H_{5/2}$ to excited $^4F_{7/2}$, $^4G_{11/2}$, as depicted in the energy level diagram in Fig. 4. It should be taken into account that only a low percentage of the Sm^{3+} ions are incorporated into the SnO_2 nanocrystals after heat treatment, due to the low solubility of the lanthanide ions in this matrix [13]. On the other hand, the broad UV band corresponds to excitation of the SnO_2 nanocrystals and subsequent energy transfer to Sm^{3+} ions [11].

This broad UV band shifts to shorter wavelengths when the SnO_2 concentration decreases, see Fig. 3, due to the increasing of the semiconductor band gap when the nanocrystal size is reduced. This change is caused by the quantum-confinement conditions and can be explained by the Brus equation:

$$E_g(R) \approx E_g(R \rightarrow \infty) + \frac{\hbar^2 \pi^2}{2R^2}\left(\frac{1}{m_e^*} + \frac{1}{m_h^*}\right),$$

where $E_g(R)$ is the energy gap of nanocrystals with radius R, $E_g(R \rightarrow \infty)$ is the bulk energy gap and m_e^* and m_h^* are the effective mass of electrons and holes, respectively [1, 10]. We will assume for SnO_2 the values $E_g(R \rightarrow \infty) = 3.6$ eV, $m_e^* = 0.27m_e$ and $m_h^* \gg m_e^*$, see [10]. Thus, an appreciable increase of the energy gap in comparison to the value for bulk samples is obtained

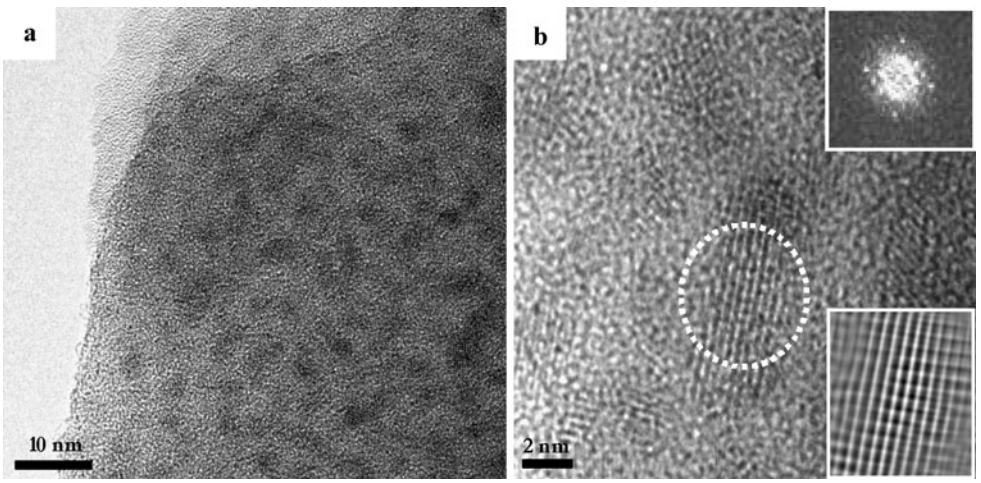

Fig. 2 (**a**) TEM bright-field image of $95SiO_2$–$5SnO_2$:$0.4Sm^{3+}$ glass-ceramic, heat treated at 900°C during 4 hours, showing the structural features of the crystalline nanophase. (**b**) HRTEM bright-field image of nanocrystalline area. *The right-top side inset* corresponds to the power spectrum obtained from the single SnO_2 nanocrystal indicated by the *white circle*. *The right-bottom side inset* corresponds to the filtered image of the same nanoparticle

when the nanocrystal radius is comparable or smaller than the Bohr's exciton radius, i.e. 2.4 nm for SnO_2 [5].

The radii calculated from the excitation spectra by using the Brus equation have been depicted in the inset of Fig. 3, together with results obtained from XRD measurements, showing a reasonable agreement among them. For samples of 3 and 5 mol% of SnO_2, the calculated radii (2.2 and 3.0 nm, respectively) are comparable to the Bohr's exciton radius. However, for 10 mol% SnO_2 samples, the mean radii calculated by the Scherrer and Brus equations (4.2 and 4.7 nm, respectively) correspond to weak confinement. Therefore, the use of the Brus equation is limited for this case due to a small gap variation versus the bulk.

The dependence of the emission spectra on the SnO_2 concentration, related to the mean nanocrystal size, is analyzed in Fig. 5. These spectra have been obtained under excitation at the maximum of the UV broad band (ranging from 320 to 340 nm for SnO_2 concentrations from 3 to 10 mol%) and also by direct excitation of the Sm^{3+} ions at 402 nm (the narrow peak observed in the excitation spectra of Fig. 3). All spectra show emission peaks of the Sm^{3+} ions, corresponding to ${}^4G_{5/2} \rightarrow {}^6H_J$ transitions with $J = 5/2$, 7/2 and 9/2, along with a SnO_2 intrinsic wide VIS emission band, with peak position ranging from 540 to 610 nm when the SnO_2 concentration increases from 3 to 10 mol%. A similar wide emission was previously observed in undoped samples [14]. The origin of this intrinsic emission is attributed to exciton recombination, mediated by deep energy levels of oxygen vacancies in SnO_2 nanocrystal, which is involved in the energy transfer to RE doping ions under interband excitation [14].

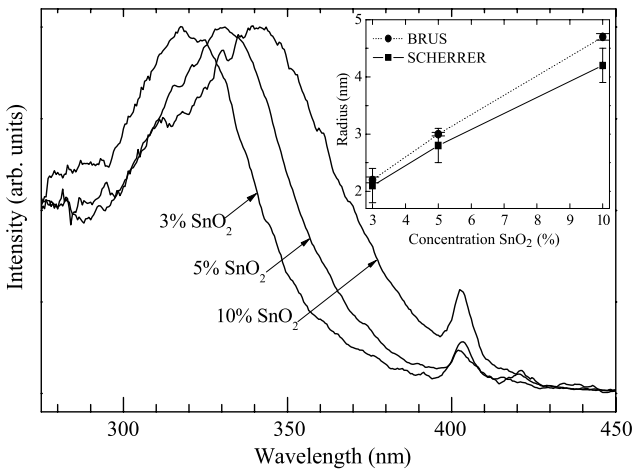

Fig. 3 Excitation spectra at room temperature detecting at 567 nm of $(100 - x)SiO_2$–$xSnO_2$:$0.4Sm^{3+}$ glass-ceramic with $x = 3$, 5 or 10 mol% of SnO_2, heat treated for 4 hours at 900°C. *Inset* shows calculated radii by the Brus and Scherrer equations as a function of SnO_2 concentration

The emission spectra obtained under direct excitation of the Sm^{3+} ions to the ${}^4F_{7/2}$, ${}^4G_{11/2}$ level, at 402 nm, show relatively broad Stark components which is indicative of a low symmetry coordination sphere for Sm^{3+} ions in a vitreous environment. Three emission peaks at 562, 600 and 648 nm are observed, corresponding to the indicated ${}^4G_{5/2} \rightarrow {}^6H_J$ transitions. It should be noticed that all the Sm^{3+} ions present in the samples can be excited by this direct pumping at 402 nm. Therefore, the observed lack of a well resolved Stark structure supports the above-mentioned hypothesis of low incorporation of Sm^{3+} ions into the precipitated SnO_2 nanocrystals [13].

There is a remarkable dependence of the emission spectra on the SnO_2 concentration under excitation into the UV broad band. For the lowest concentration samples; i.e. 3 mol%, relatively small SnO_2 nanocrystals are excited, presenting a spectrum characteristic of Sm^{3+} ions in a vitreous environment. In these small nanocrystals the Sm^{3+} ions are close to the surface, where distorted environments and interaction with the SiO_2 glassy surrounding could explain the obtained spectrum. When the SnO_2 concentration is in-

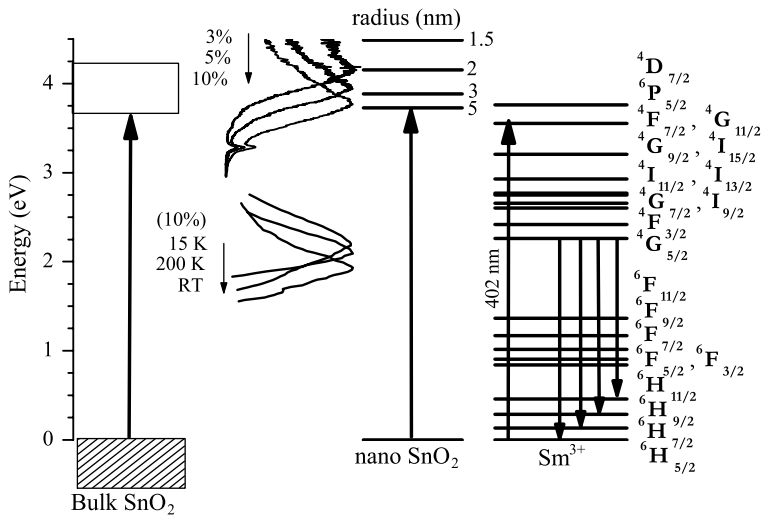

Fig. 4 Energy level diagram of Sm^{3+} ions where main excitation and emission transitions are indicated. The energy gap of SnO_2 for bulk and nanocrystals is also depicted. For SnO_2 nanoparticles, the lowest discrete energy levels in the conduction band for different values of nanocrystal radii, obtained with different SnO_2 concentrations, are indicated. Broad UV excitation peaks for 3, 5 and 10 mol% of SnO_2 and broad VIS emission for 10 mol% of SnO_2 at 15 K, 200 K and room temperature have also been included

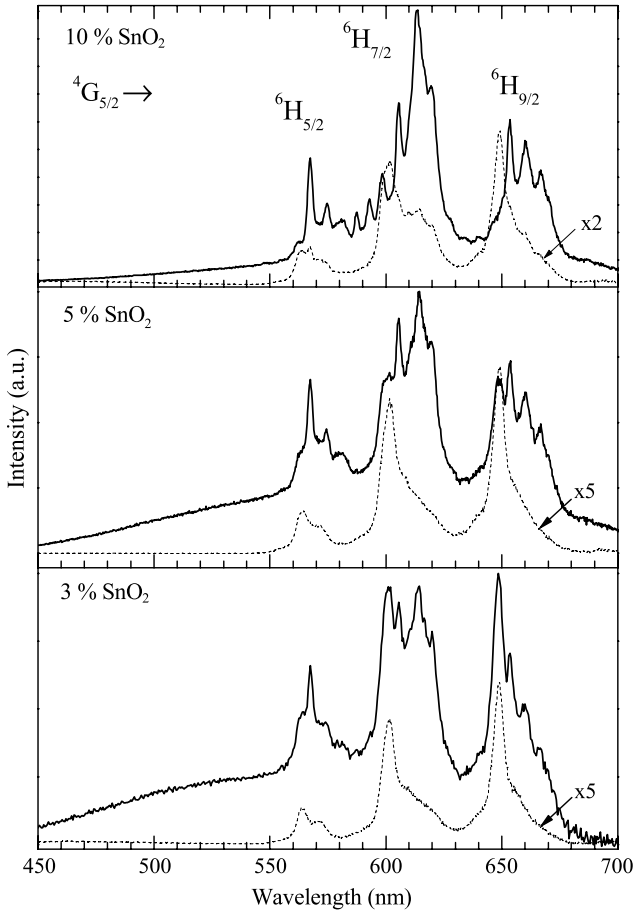

Fig. 5 Emission spectra at room-temperature excitation at 402 nm (*dash line*) and at the maximum of the UV broad band (*solid line*) of $(100-x)SiO_2$–$xSnO_2$:$0.4Sm^{3+}$ glass-ceramics, with $x = 3$, 5 or 10 mol% of SnO_2, heat treated for 4 hours at 900°C

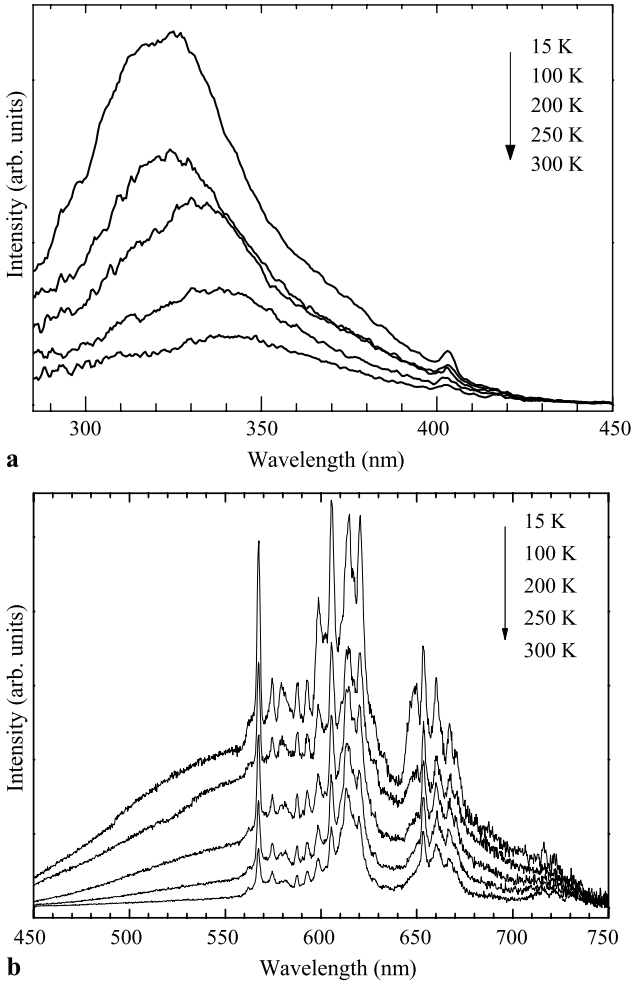

Fig. 6 Excitation spectra of $90SiO_2$–$10SnO_2$:$0.4Sm^{3+}$ (mol%) glass-ceramics (**a**) detecting the Sm^{3+} emission at 567 nm for temperatures ranging from 15 K to room temperature and (**b**) corresponding emission spectra excitation at the maximum of the UV broad band for each temperature

creased, emission peaks show better-resolved Stark structure, indicating a more crystalline environment for the Sm^{3+} ions related to the nanocrystal size increase, already discussed above from XRD and excitation luminescence data. Moreover, the intensity ratio of the ${}^4G_{5/2} \rightarrow {}^6H_{7/2}$ to the ${}^4G_{5/2} \rightarrow {}^6H_{9/2}$ transition clearly increases with the SnO_2 concentration from 3 to 10 mol%, confirming the enhancement of crystallinity.

With the aim of obtaining additional information about mechanisms underlying energy transfer processes from SnO_2 nanocrystals to Sm^{3+} ions, the dependence of the luminescence on temperature has been analyzed from 15 K to room temperature. Thus, Fig. 6(a) shows excitation spectra of $90SiO_2$–$10SnO_2$:$0.4Sm^{3+}$ mol% samples heat treated at 900°C during 4 h detecting the Sm^{3+} emission at 567 nm, ${}^4G_{5/2} \rightarrow {}^6H_{5/2}$ transition. A blue shift, from 340 to 320 nm, together with intensity increasing is observed in the excitation UV broad band with lowering temperature. Corresponding emission spectra are shown in Fig. 6(b), they were obtained under excitation at the maximum of the UV broad band for each temperature, i.e. exciting an equal size nanocrystal set. The intensity of both, Sm^{3+} and VIS broad emission increases when the temperature is lowered. It is observed that this VIS broad emission is near completely quenched at room temperature, whereas a large fraction of the Sm^{3+} emission prevails when the temperature is increased.

There are different factors which affect the temperature dependence of these emissions. On one hand, when the temperature is increased, the probabilities of non-radiative transitions enhance and the radiative de-excitation pathways prevail (taking into account that radiative probabilities are not significantly affected by temperature). On the other hand, the energy transfer processes from the nanocrystal host to the Sm^{3+} ions, which lead to emission of these ions under UV excitation, would be favored by lowering the temperature. This can be concluded from Fig. 4, which shows that the overlap of the VIS broad emission (extracted from emission spectra of Fig. 6(b)) with the upper-lying

emitting levels of the Sm^{3+} ions increases at low temperature. In this sense, the non-resolved Stark structure luminescence peak at 600 nm, corresponding to Sm^{3+} ions close to the surface of the SnO_2 nanocrystals as was observed in Fig. 5, enhances appreciably when lowering temperature due to above-mentioned effects.

Finally, it should be also noticed that SnO_2 presents a high concentration of neutral oxygen vacancies that act as electron donors. On the other hand, when this semiconductor is doped with rare-earth ions RE^{3+} substituting Sn^{4+}, charge compensation results in single ionized oxygen vacancies. From here, the emission remaining at room temperature under UV interband excitation would proceed from oxygen vacancies with charge compensated by close Sm^{3+} ions.

4 Conclusions

Sol-gel nano-glass-ceramics comprising Sm^{3+}-doped SnO_2 wide band-gap semiconductor quantum-dots dispersed in silica matrix have been successfully obtained for different SnO_2 concentration. Calculated nanoparticle mean radius points to a strong quantum-confinement regime. Room-temperature luminescence is noticeably enhanced when doping with Sm^{3+} ions, which are efficiently excited through energy transfer from the SnO_2 host. Moreover, evolution of the luminescence as a function of SnO_2 concentration indicates a dependence on the nanoparticle dimension, due to selective excitation of nanocrystal sets with predetermined size. Finally, a study of the luminescence as a function of temperature has been carried out, elucidating underlying energy transfer mechanisms related to overlapping between SnO_2 broad VIS emission and emitting levels of Sm^{3+} ions.

Acknowledgements The authors would like to thank Agencia Canaria de Investigación, Innovación y Sociedad de la Información y Fondo Europeo de Desarrollo Regional (FEDER) (PIL2260902) and Ministerio de Ciencia e Innovación of Spain Government (MAT2009-12079).

References

1. E. Brus, J. Chem. Phys. **80**, 4403 (1984)
2. A. Henglein, Chem. Rev. **89**, 1861 (1989)
3. M. Nogami, T. Enomoto, T. Hayakawa, J. Lumin. **97**, 147 (2002)
4. F. Gu, S.F. Wang, M.K. Lu, Y.X. Qi, G.J. Zhou, D. Xu, D.R. Yuan, Opt. Mater. **25**, 59 (2004)
5. A.C. Yanes, J. del-Castillo, M.E. Torres, J. Peraza, V.D. Rodríguez, J. Méndez-Ramos, Appl. Phys. Lett. **85**, 2343 (2004)
6. J. del-Castillo, V.D. Rodríguez, A.C. Yanes, J. Méndez-Ramos, Nanotechnology **16**, 303 (2005)
7. S. Brovelli, A. Chiodini, A. Lauria, F. Meinardi, A. Paleari, Phys. Rev. B **73**, 406 (2006)
8. J. del-Castillo, V.D. Rodríguez, A.C. Yanes, J. Méndez-Ramos, J. Nanopart. Res. **10**, 499 (2008)
9. J. del-Castillo, A.C. Yanes, J.J. Velázquez, J. Méndez-Ramos, V.D. Rodríguez, J. Alloys Compd. **473**, 571 (2009)
10. N. Chiodini, A. Paleari, D. Di Martino, G. Spinolo, Appl. Phys. Lett. **81**, 1702 (2002)
11. A.C. Yanes, J.J. Velázquez, J. del-Castillo, J. Méndez-Ramos, V.D. Rodríguez, Nanotechnology **19**, 295707 (2008)
12. A. Patra, D. Kundu, D. Ganguli, Mater. Lett. **32**, 43 (1997)
13. E.A. Morais, S.J.L. Ribeiro, L.V.A. Scalvi, C.V. Santilli, L.O. Riggiero, S.H. Pulcinelli, Y.J. Messaddeq, J. Alloys Compd. **344**, 217 (2002)
14. J. del-Castillo, A.C. Yanes, J. Méndez-Ramos, V.D. Rodríguez, J. Nanosci. Nanotechnol. **8**, 2143 (2008)